Elucidating the performance and unexpected stability of partially coated water-splitting silicon photoanodes

Kiseok Oh, Cristelle Mériadec, Benedikt Lassalle-Kaiser, Vincent Dorcet, Bruno Fabre, Soraya Ababou-Girard, Loïc Joanny, Francis Gouttefangeas, Gabriel Loget

Elucidating the Performances and Unexpected Stability of Partially Coated Water-Splitting Silicon Photoanodes

Kiseok Oh,[a] Cristelle Meriadec,[b] Benedikt Lassalle-Kaiser,[c] Vincent Dorcet,[a] Bruno Fabre,[a] Soraya Ababou-Girard,[b] Loic Joanny,[d] Francis Gouttefangeas[d] and Gabriel Loget*[a]

H_2 is an ideal energy carrier because it has a high energy density, it can be easily stored, transported, and readily used to power electrical devices. Like photosynthesis, where photons are converted into energy-rich molecules, sunlight energy can be converted into H_2 and O_2 using photoelectrochemical water splitting cells (PECs). Despite the fact that silicon is considered one of the most attractive semiconductors for manufacturing photoelectrodes, its use is currently limited by its low activity and its instability in aqueous solutions. Herein, we report on surprisingly stable Si-based photoanodes, fabricated by simple aqueous electrodeposition, which results in the partial (< 20%) coating of the Si surface with dispersed Ni nanoparticles (NPs). We show that photoelectrochemical activation considerably improves their performances by generating a high-activity catalytic shell around the Ni NPs. In addition, we demonstrate the stability of the photoanodes under various conditions in highly corrosive alkaline solutions in operation and in inactivity. The protection in operation is explained by anodic passivation, which generates a stabilizing SiO_x layer. In contrast, the stability when no polarization is applied is unexpected because most of the Si, highly prone to etching, is in contact with the very corrosive aqueous phase. The experimental data allows us to propose a mechanism explaining this effect.

Introduction

The conversion of sunlight in H_2 is a clean alternative to fossil fuels for producing energy on-site and on-demand.[1] This process can be achieved by photoelectrochemical cells (PECs), devices composed of semiconductor (SC) absorbers, immersed in an aqueous electrolyte, which can convert solar energy in pure H_2.[2,3] Under sunlight irradiation PECs absorb photons and convert them into charge carriers that are driven at the solid–liquid interface to react with water, generating simultaneously pure H_2 and O_2.[4–8] Several monolithic PECs have been reported and operated with reasonable conversion efficiencies[9] but their practical use will only be conceivable when their cost will be reduced and their stability will be improved.[3,9]

To be used in PECs, light absorbers must own several physical properties, such as a short band gap to absorb a significant part of the solar spectrum, high carrier mobilities, and low recombination rates. In addition to meeting these criteria, silicon (Si) is nontoxic, abundant and widely used by the photovoltaic industry, which makes it the most attractive material for PEC manufacturing.[10] Employing Si as a photoelectrode remains, however, a challenge for two main reasons. First, hydrogen evolution reaction (HER) and oxygen evolution reaction (OER) are sluggish at the Si-liquid interface and require considerable overpotentials to occur, therefore the immobilization of co-catalysts (*cocats*) at the Si surface is essential to increase reaction kinetics and lower the energy input. This implies stringent constraints in terms of material cost as well as a fine surface engineering strategy to preserve the light absorption and energetics of the photoelectrode.[10] Second, as the self-oxidation potential of Si (-0.99 V *vs* normal hydrogen electrode NHE) is much more negative than the standard potential of O_2/H_2O (+1.23 V *vs* NHE), the oxidation of Si into insulating SiO_x is the main process occuring at Si photoanodes,[11,12] which leads to their quasi-spontaneous deactivation when used for water splitting.[13,14] In addition, the instability of this material is even more pronounced in alkaline media due to the well-known chemical etching that happens spontaneously on Si and Si oxides at ambient conditions.[15–17] If these crucial issues had restrained the development of efficient Si-based photoanodes for the last decades, tremendous progress on photoanode protection has been recently achieved.[13,14] Protection strategies imply in almost all cases the introduction of a conformal layer (*e.g.* TiO_2 or indium tin oxide) between Si and the *cocat*, deposited by vapor deposition[18–23] or atomic layer deposition.[24–29] Using these methods (considered as expensive and time-consuming) for PEC manufacturing may limit the possible designs because building up thin conformal layers on non-planar SCs (which can

[a] *Univ Rennes, CNRS, ISCR (Institut des Sciences Chimiques de Rennes)-UMR6226, F-35000 Rennes, France.*
[b] *Univ Rennes, CNRS, IPR (Institut de Physique de Rennes)-UMR6251, F-35000 Rennes, France.*
[c] *Synchrotron SOLEIL, L'Orme des Merisiers, Saint-Aubin, 91192 Gif-sur-Yvette, France.*
[d] *Univ Rennes, CNRS, ScanMAT-CMEBA –UMS2001, F-35000 Rennes, France.*
Electronic Supplementary Information (ESI) available: [details of any supplementary information available should be included here]. See

be beneficial for improving the performances)[30] is a technological challenge.

A handful of recent reports by our group[31] and others[32–34] have demonstrated that, despite the notorious instability of Si in water, OER can be performed for relatively long times (up to 40 h) in strongly alkaline media with Si photoanodes partially covered with Ni-[31] or Co-based electrodeposits.[32] This behavior is particularly surprising because in these cases the majority of the Si surface is in direct contact with the corrosive environment. Besides being intriguing from a fundamental point of view, this phenomenon may also be highly important for the manufacturing of Si-based PECs because it relies on low-cost electrodeposition, which can be readily up-scaled.[35] Yet, it is crucial to understand this unexpected behavior that may lead to breakthroughs in protection strategies for photoelectrodes.[36]

On the other hand, while PECs are also subject to degradation mechanisms when electrolysis is not occurring (*e.g.* during the night), the stability of photoanodes is almost exclusively tested under operating conditions.[37] The question of the stability of unpolarized photoelectrodes is particularly relevant in the case of low bandgap semiconductors in harsh environments, and Si photoanodes partially coated with nanoparticles (NPs) have only been studied under operation.[31–34]

Here, we report on high-activity Si photoanodes prepared by a simple low-cost process. We first study their photoelectrochemical activation, which considerably improves their performance. We demonstrate then that illumination, as well as operation, drastically affects their stability and we show that they can be exposed to alkaline electrolytes for long periods of time, even when inactive. Finally, based on electrochemical and electron microscopy data, we discuss the mechanisms that explain such a stability.

Results and discussion

High-performance *n*-Si photoanodes decorated by Ni or Co NPs are considered metal-insulator-semiconductor (MIS) junctions operating in the "pinch-off" regime[38–40] (a scheme is shown in the inset of Figure 1a). This regime is extremely beneficial because it takes advantage of the metal-free regions to generate a high photovoltage and the metal-Si junction to create a low resistance pathway for photogenerated minority carriers, which are readily injected into the metal *cocat* for water oxidation. In this work, dispersed hemispherical Ni^0 NPs were deposited on *n*-Si (100) by cathodic electrodeposition from an aqueous solution (see SI for more details). Our process led to an NP surface coverage of 18% (Figure S1) indicating that most of the Si surface was uncovered by Ni. Nonetheless, as the modification took place under ambient conditions, the exposed Si surfaces were covered by a thin SiO_x oxide layer.[15]

The anodic behavior of such surfaces in 1 M NaOH (measured pH = 13.6) is shown by the linear sweep voltammograms (LSVs) of Figure 1a (Figure S3a presents the corresponding cyclic voltammograms (CVs)). Negligible currents were obtained in the dark whereas, under simulated sunlight, substantial oxidation photocurrents were measured. In all case except for the freshly-prepared photoanode, a redox wave attributed to the Ni^{III}/Ni^{II} redox couple first appeared,[41,42] followed by a higher OER current accompanied by O_2 bubble evolution, according to reaction (1):

$$4\ OH^-\ (l) + 4\ h^+ \rightarrow O_2\ (g) + 2\ H_2O\ (l) \qquad (1)$$

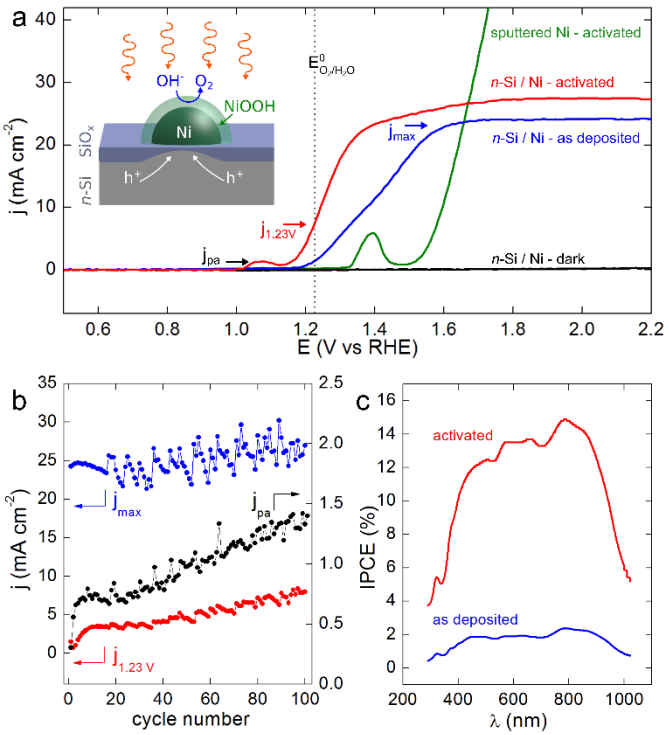

Fig. 1. a) LSVs recorded under AM 1.5G illumination for a photoanode before (blue) and after (red) activation. LSVs recorded in the dark and after electrochemical activation for a photoanode (black) and a sputtered Ni thin film (green). Inset: scheme showing a cross-section of the pinched-off MIS photoanode under operation. b) Evolution of $j_{1.23V}$ (red), j_{pa} (black) and j_{max} (blue) during activation. IPCE spectra recorded at +1.23 V for *n*-Si modified with Ni NPs before (blue) and after (red) activation. All curves were recorded in O_2-saturated stirred 1 M NaOH at 100 mV s^{-1}, except for the green LSV that was recorded at 20 mV s^{-1} (see Figure S4a for more details).

Photoelectrochemical activation

Photoelectrochemical conditioning, achieved by imposing hundred successive voltammetric cycles under illumination (Figure S3b), led to a gradual improvement of the photoanode performance. This can be noticed by comparing the LSV recorded at the first cycle (blue) with the one recorded at the hundredth cycle (red), respectively. In the following, we will refer to this process as activation. Activating by electrochemical cycling is particularly relevant here as it allows a fine *in-situ* measurement of several benchmark parameters at each successive cycle, namely: the light-limited photocurrent density (j_{max}), the photocurrent density at the standard potential (E^0) of the O_2/H_2O couple ($j_{1.23V}$) and the one at the Ni^{III}/Ni^{II} oxidation peak (j_{pa}).

The evolution of these parameters during activation is shown in Figure 1b. First, one can observe that j_{pa}, which was almost zero at first, gradually increased. As this redox wave corresponds to the oxidation of $Ni(OH)_2$,[41,42] it demonstrates that the activation process transformed a part of the Ni^0 NPs

into a redox active $Ni(OH)_2$ species. During this wave, $Ni(OH)_2$ was converted into NiOOH, according to reaction (2):

$$Ni^{II}(OH)_2\ (s) + OH^-\ (l) + h^+ \rightarrow Ni^{III}OOH\ (s) + H_2O\ (l) \qquad (2)$$

NiOOH (in particular, its γ- phase) is commonly presented as the catalytically-active phase for OER in Ni-based compounds,[43,44] it is thus considered here as the *cocat*. After this redox wave, the OER photocurrent increased with a slope dependent on the reaction kinetics (Figure 1a). The red curve of Figure 1b shows a striking increase of $j_{1.23V}$ (> 5 fold), demonstrating that the conversion efficiency was considerably improved by the activation. This effect was further confirmed by the incident photon-to-current conversion efficiency (IPCE) spectra recorded at +1.23 V (Figure 1c). In addition, activation also increased j_{max} by 11%, as revealed by the blue curve of Figure 1b. To sum up, activation led to photoanodes with j_{pa}, $j_{1.23V}$ and j_{max} values of 1.12 ±0.3, 7.8 ±2.4 and 27.9 ±3.9 mA cm^{-2}, respectively, as based on measurements obtained on ten individual photoanodes. Figure 1a also presents an LSV obtained for a sputtered, 100 nm-thick, Ni thin film (green curve), activated using the same procedure as described before (Figure S4b). The comparison between the green and the red curves indicates that the activated photoanode triggered OER at an onset potential negatively shifted by 0.36 V (Figure S9) with respect to the non-photoactive Ni surface.

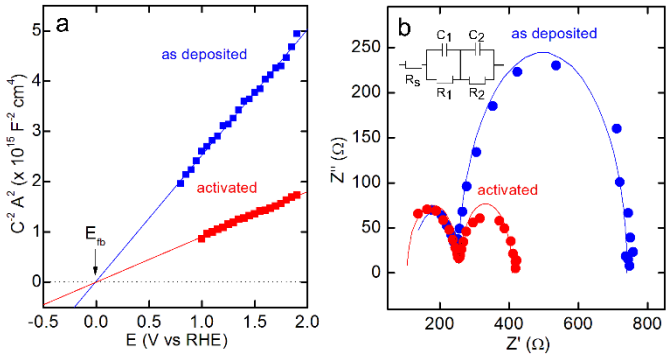

Fig. 2. a) MS plots recorded at 2 kHz for an anode before (blue) and after (red) activation, squares are experimental points and lines are linear fits. b) Nyquist plots recorded at +1.23 V under AM 1.5G illumination, disks are experimental points and lines are fits of the equivalent circuit shown in the inset. All curves were recorded in O_2-saturated stirred 1 M NaOH.

Several hypotheses can be drawn regarding the origin of the performance increase during activation: it could be induced by a variation of the energetics of the photoanode or by an improved electrocatalysis at the *cocat*/electrolyte interface. In order to gain further insights into these aspects, electrochemical impedance spectroscopy (EIS) measurements were carried out. First, Mott-Schottky (MS) plots shown in Figure 2a reveal that the flat band potential E_{fb} did not change after the activation process, suggesting that the performance improvement was not induced by its shift. Additionally, the Nyquist plots show two semi-circles in the frequency range of 120 kHz - 0.1 Hz (Figure 2b) with the diameter of the second semi-circle being strongly decreased after activation. These curves were reasonably fitted using the equivalent electrical circuit depicted in the inset,[33,45] which includes the resistances and capacitances associated with the charge transfers processes at the *cocat*/electrolyte interface (R_1, C_1) and in the solid phase (R_2, C_2) as well as the solution resistance (R_s). The fits (Table S2) revealed a considerable decrease of the charge transfer resistance R_1 after activation (>3 fold) as well as an increase of C_1 (6 fold). This behavior is well in line with an improved hole transfer caused by the generation of the catalytic NiOOH-$Ni(OH)_2$ phase at the Ni/electrolyte interface during activation.

Characterization of activated photoanodes

The effect of activation was also investigated by scanning and transmission electron microscopy (SEM and TEM) as well as atomic force microscopy (AFM). SEM pictures of an as-deposited and an activated surface are shown in Figure 3a,b and Figure S2, respectively. Analysis of the size distribution (Figure S6) indicated that the Ni NPs before activation had an average diameter of 60 ±36 nm. The NP height, measured on cross-sectional views such as the one of Figure 3b, was 30 ±8 nm, which was confirmed by AFM measurements (average NP height = 33 ±9 nm, Figures 3c and S12). SEM did not allow to observe a significant change of the geometrical parameters after activation, except for the NP mean diameter that increased by 5% (63 ±42 nm, Figure S6), due to volume expansion associated with the oxidation of the Ni NPs.

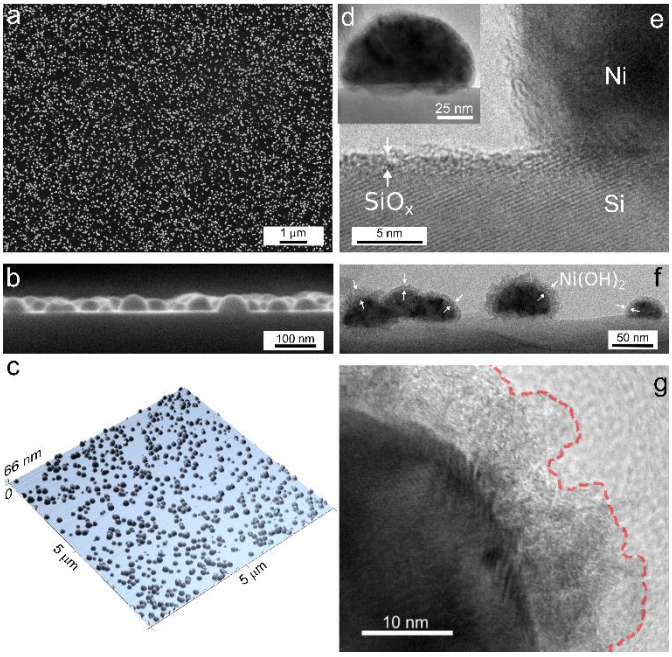

Fig. 3. a) SEM top view showing the surface of a photoanode before activation. b) Corresponding SEM cross-sectional view. c) Corresponding AFM image. d) TEM and e) HR TEM images of a single Ni NP electrodeposited on *n*-Si. f) TEM and g) HR TEM images obtained after activation of the surface, the external boundary of the NP shell is indicated by a dashed red line.

In contrast, TEM gave clear information about the NP morphology. Figure 3d,e shows a single Ni NP on Si after deposition. The Ni NPs were polycrystalline with a selected area electron diffraction (SAED) pattern corresponding to Ni^0 (Figure S15a). High-resolution (HR) TEM observations revealed

that the Si surface was coated with an amorphous layer of SiO_x having a thickness in the range of 1 nm (Figure 3e). After activation, the outer surface of the Ni NPs (*i.e.* the one exposed to the electrolyte) drastically changed. As shown in Figure 3f,g, all NPs were encapsulated by a ~10 nm-thick rough and polycrystalline shell. The SAED pattern of an individual NP after activation (Figure S15b) shows three spots which confirm the presence of Ni^0 and $Ni(OH)_2$, indicating that the shell was composed of the $Ni(OH)_2$ pre-catalytic phase, that formed during activation, as previously assumed based on the electrochemical measurements (*vide supra*). In addition, this figure reveals two rings that may be ascribed to $Ni(OH)_2$, γ-NiOOH and/or NiO. If the presence of γ-NiOOH and NiO is uncertain, these phases could exist on the NPs, the first one, in the shell, as a product of reaction (2) and the latter one, at the interface between Ni^0 and the shell.[41]

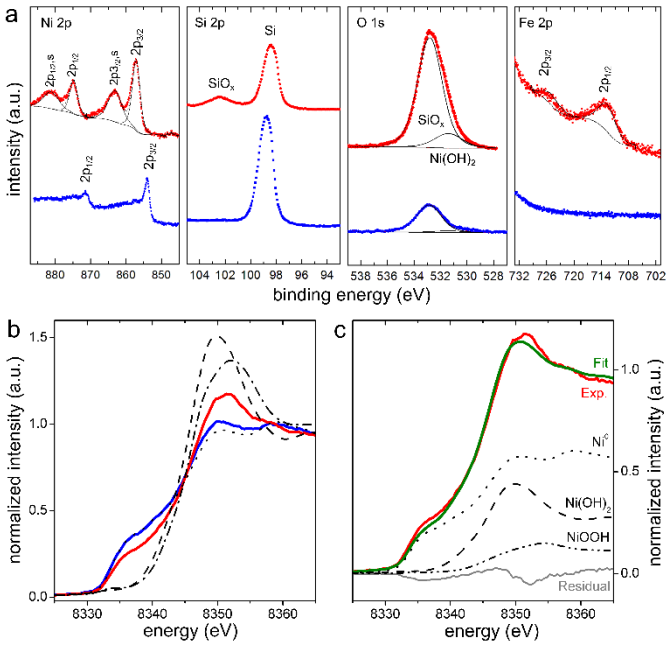

Fig. 4. a) XPS spectra showing the Ni 2p, Si 2p, O 1s and Fe 2p regions, measured for the as-deposited (blue) and activated (red) photoanodes. The three first spectra were recorded with an Al source and the fourth one with an Mg source. Fits and Shirley backgrounds are represented by black thin lines. b) XANES spectra at the nickel K-edge of as-deposited (blue) and activated (red) samples and of the reference compounds metallic Ni^0 (black dotted), $Ni(OH)_2$ (black dashed) and γ-NiOOH (black dash-dotted). c) linear combination fitting of the activated sample showing the experimental data (red), the weighted spectra of the Ni^0 (black dotted), $Ni(OH)_2$ (black dashed) and γ-NiOOH (black dashed-dotted) references, the fit (green) and the residual difference (grey) between the experimental data and the fit.

X-ray photoelectron spectroscopy (XPS) measurements were performed on surfaces after preparation and after activation. The survey spectra (Figure S16), confirmed the presence of the expected elements: Si, O, Ni as well as Na for the activated electrode, the latter being probably integrated into the NP shell during activation. Several regions of particular interest are reported in Figure 4a. Before activation, the Ni 2p region exhibited the characteristic shape for Ni^0 with $2p_{3/2}$ and $2p_{1/2}$ peaks at respective binding energies of 853.8 and 871.3 eV, which is in good agreement with what has been reported for Ni^0 thin films.[46,47] After activation, the XPS signal changed considerably and could be fitted with four broad components at binding energies of 857.1, 863.2, 874.7 and 881.3 eV, values in good agreement with the Ni $2p_{3/2}$, the $2p_{1/2}$ peaks and the satellite peaks commonly observed for $Ni(OH)_2$[48] and NiOOH (these compounds can be hardly differentiated by XPS),[49] which corroborate our electrochemical and TEM data. Only one Si 2p peak was detected on the as-prepared surface, at 98.8 eV, which corresponds to lattice Si. After activation, the intensity of this peak decreased and an additional one appeared at 102.5 eV, demonstrating the extension of the SiO_x layer during electrochemical activation.[50]

These measurements are in very good agreement with the evolution of the signals observed in the O 1s region, where a considerable increase of the peak at 532.9 eV was observed after activation. In addition, the O 1s broad peak could eventually be fitted with two components, the largest corresponding to SiO_x and the second one, at 531.5 eV, to $Ni(OH)_2$.[48] Careful examination of the Fe 2p region was quite interesting, indeed, even if the four survey spectra of Figure S16 did not indicate the presence of this element, we intentionally performed high count rate measurements with a Mg source (in order to avoid the Ni Auger peaks in the Fe 2p region), which revealed small peaks at 713.3 and 726.3 eV, demonstrating the presence of Fe on the surface. Fe was only observed after activation, which confirms that its incorporation originates from this treatment. Based on the XPS data, the Fe to Ni ratio in the NP shell was evaluated to 0.14. The presence of Fe in the catalytic phase is particularly relevant as it has been clearly documented that adventitious Fe incorporates in $Ni(OH)_2$ and NiOOH during electrochemical experiments.[51] Although the precise role of Fe in NiOOH catalysts is still under debate,[52–54] it is known to have a considerable influence on the activity of Ni-based OER electrocatalysts.[55,56]

X-ray absorption near edge spectra (XANES) were recorded at the Ni K-edge on a sample after deposition and after electrochemical activation. Figure 4b,c shows the XANES spectra of these two surfaces, together with reference samples. A first observation indicates that the sample before activation is very close to metallic Ni, while the one after activation presents features reminiscent of Ni oxides (intense white line at 8350 eV). We performed linear combination fittings (Table S1) on these two samples using the reference spectra shown in Figure 4b. Although the as-deposited sample can be fit with a *ca.* 10% contribution of Ni^{II}, a contribution from one of the NiOOH phases is required to reproduce the spectrum of the sample after activation. Figure 4c shows a fit that was obtained with a $Ni^0/Ni(OH)_2/$γ-NiOOH composition of 64:29:11. Although the figures of merit of the fits cannot rule out the presence of NiO and/or β-NiOOH, it is clear that contributions from both Ni(II) and Ni(III) components are required to reproduce the experimental spectrum.

To sum up, electrochemical data, TEM, XPS and XANES measurements revealed that photoelectrochemical activation induced Si oxidation and generated a $Ni(OH)_2$-NiOOH catalytic shell doped with Fe atoms over the Ni^0 NPs.

Stability during operation

After having characterized our photoanodes and described the effect of electrochemical activation, we will now discuss their stability, first, in operation and, in the following section, under unbiased conditions.

Figure 5a shows the chronoamperometry (CA) curves obtained for two activated photoanodes during prolonged electrolysis at different potentials. When the polarization was positive enough (+2.9 V), the photoanodes delivered the photocurrent density corresponding to j_{max}, as defined in Figure 1, and operated with a quantitative OER faradaic efficiency (inset of Figure 5a). The current was stable for several hours and the stability time (defined here as the time during which j remains >90% of the initial j) was 11 h. Performing the electrolysis with a smaller overpotential (at $E^0_{O2/H2O}$) led to a more interesting situation that is presented in the red curve of Figure 5a. The photoanode first delivered $j_{1.23}$, then the photocurrent increased during the 8 first hours and, finally, decayed. In order to understand this phenomenon, LSVs were recorded at different electrolysis times, as shown in Figure 5b. These curves demonstrate that the OER onset potential shifted negatively during the photocurrent rising period and that the surface was totally deactivated after 20 h of operation. The stability time was, in this case, 14 h, and the faradaic efficiency 92%.

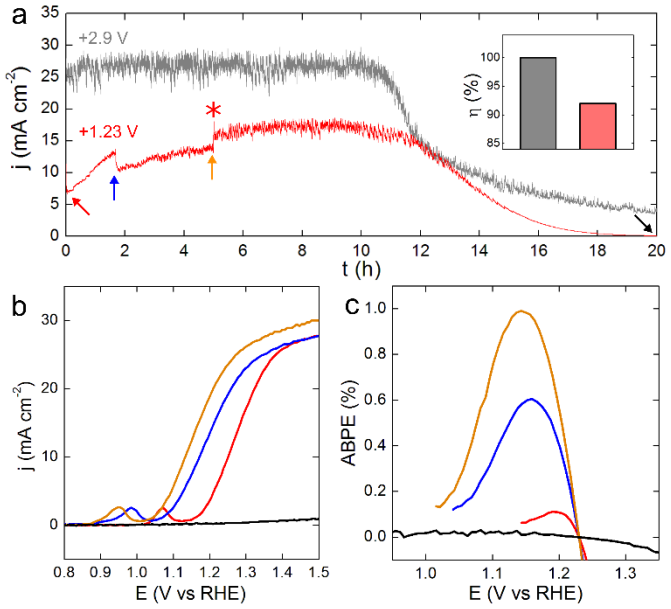

Fig. 5. a) CAs curves recorded during prolonged photoelectrolysis for activated photoanodes that were held at +2.9 V (grey) and +1.23 V (red), the asterisk indicates when bubbles were removed from the surface, the colored arrows indicate when LSVs were performed. Inset: corresponding OER faradaic efficiencies. b) LSVs recorded under AM 1.5G illumination at t = 0 , 1.7 , 5 and 20 h during the photoelectrolysis at +1.23 V, as indicated by the colored arrows in Figure 5a. c) ABPE curves corresponding to the LSVs shown in Figure 5b.

In addition, the evolution of the photoanode performance over the electrolysis can be clearly observed in the applied bias photon-to-current efficiency curves (ABPE). According to Figure 5c, the ABPE maximum, which was in all cases comprised between +1.1 and +1.2 V, varied from an initial value of 0.1% to 1% at 7 h. This considerable improvement is attributed to the *in-operando* activation of the photoanode induced by the increase of the catalytic shells around the Ni NPs. This is confirmed by the increase of the charge under the Ni^{III}/Ni^{II} oxidation wave, which varied from an initial value of 0.13 to 0.30 mC cm^{-2} at 5 h. The gradual deactivation of the photoanode is corroborated with the removal of the NPs that was clearly observed by SEM (Figures 8b and S17). Interestingly, the Si surface did not exhibit etching pits after such a long electrolysis. Indeed, pits are supposed to develop as a result of the fast and spontaneous chemical etching when a Si surface is immersed in an alkaline solution,[15] as described by the following reaction:

$$Si\ (s) + 2\ H_2O\ (l) + 2\ OH^-\ (l) \rightarrow SiO_2(OH)_2^{2-}\ (l) + 2\ H_2\ (g) \qquad (3)$$

The absence of etching during electrolysis can be ascribed to the anodic protection of the Si surface that we will describe in details in the following.

Anodic passivation is clearly illustrated by the black CVs of Figure 6 that shows the electrochemical behavior of bare Si undergoing alkaline etching in the electrolyte used for electrolysis. The anodic wave that appeared at the first cycle corresponds to the formation of an oxide layer which electrically passivated the surface,[15] as revealed by the vanishing of current, obvious at the subsequent scans. This wave is characterized by the potential at which the current is maximum, *i.e.* the passivation potential (PP),[17,57,58] here, +0.06 V as indicated in Figure 6. Because the electrolysis of Figure 5a was performed at potentials more than 1 V positive from the PP, we can clearly state that the Si in operating photoanodes was coated by an anodic SiO_x layer, in good agreement with the scheme presented in the inset of Figure 1a. The etching rate of anodic Si oxides being more than two orders of magnitude smaller than the one for Si in alkaline solutions,[15] protection occurred during photoelectrolysis and the Si surface was preserved from chemical etching.

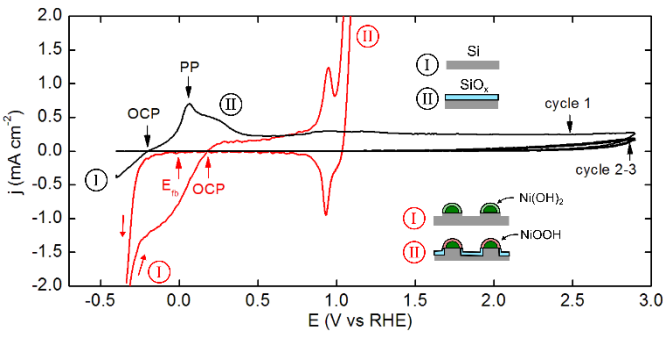

Fig. 6. CVs recorded under illumination for an *n*-Si surface undergoing alkaline etching in 1 M NaOH (black) and an activated photoanode after the etching of SiO_x (red). The positions of the OCP, the PP, and the E_{fb} determined in Figure 2a are indicated by arrows; the small arrows in the bottom left corner indicate the sweep direction. Inset: schemes depicting the cross-section of the surfaces in the regions of potential indicated on the CVs.

If anodic passivation can be quite efficient to protect Si-based photoanodes during operation, it is expected to be totally inefficient for non-polarized surfaces, *i.e.* at the open-circuit potential (OCP), because, in this case, the protective oxide is

not renewed. Indeed, although SiO_x etching is much slower than Si, SiO_x is also subjected to alkaline etching,[15] which should irremediably result in the exposure of the Si surface to the electrolyte and should cause its subsequent degradation following reaction (3).

Stability at the open-circuit potential

In order to investigate the stability of the photoanodes when not active for OER, we studied their behavior under the same conditions as those used for electrolysis, except that they were unbiased (Figure 7). We will first discuss the control experiments that are shown in Figure 7b. The OCP of an oxide-free Si surface undergoing etching (black curve) was relatively stable with a value of -0.18 V, in good agreement with the one determined by the black CV of Figure 6. In contrast, the OCP of a Si surface covered with a native SiO_x layer (blue curve) first dropped and stabilized at -0.18 V after 0.6 h, when the oxide was fully removed and etching of bare Si started following reaction (3).

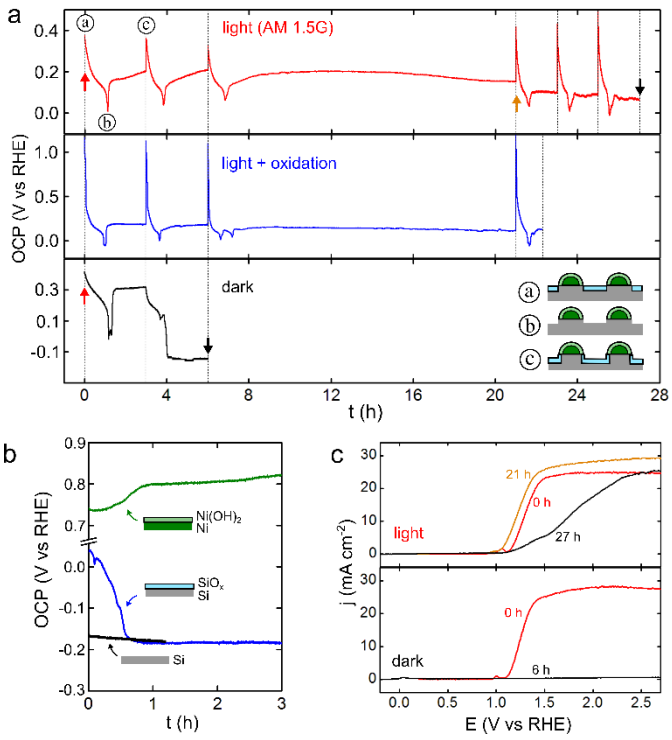

Fig. 7. a) Graphs showing the evolution of the OCP of activated photoanodes recorded: under illumination (red), under illumination with the photoelectrode being held at +2.9 V for 1 min after each CV (blue) and in the dark (black). CVs were recorded at the times indicated by the vertical dotted lines. Inset: scheme depicting the cross-section of the surface at the times indicated in the left part of the red curve (the color code is the same as in Figure 6). b) Graphs showing the evolution of the OCP under illumination for an HF-treated *n*-Si surface (black), for a SiO_x-covered *n*-Si surface (blue) and in the dark for an activated Ni thin film (green). c) LSVs recorded under illumination at the times indicated by arrows during the OCP measurements in the red (top) and the black (bottom) curves of Figure 7a.

In the experiments of Figure 7a, the OCP of freshly activated photoanodes was recorded as a function of time, CVs were regularly recorded in order to evaluate the photoanodes performance and the experiments were stopped when they exhibited clear signs of degradation. One can note that the OCP variation always followed a similar trend after activation or after recording a CV: it decreased sharply to a minimum value of ~0 V and quickly increased to a more stable value, thus leading to a dip followed by a plateau. This type of profile is generally controlled by the etching of the SiO_x layer and OCP dips are commonly attributed to the dissolution of the Si/SiO_x transition layer.[58–61] In all cases, the first dip appeared around 1 h of immersion and the subsequent dips were recorded at an average time of 0.7 h after the CV. Ellipsometry measurements revealed that the thickness of the SiO_x layer on an activated, Ni-free *n*-Si surface was 2.3 nm (surface conditioned with 100 CV cycles in 1 M NaOH under illumination). By considering this value as the thickness of the SiO_x layer on the photoanodes after activation, 1 h of exposure to the 1 M NaOH solution would result in an etching rate of 6 $x10^{-4}$ nm s^{-1}, which is in very good agreement with the reported values (anodic oxides are known to be etched at 1 $x10^{-3}$ nm s^{-1} in 2 M KOH).[15,58] This confirms that the dip apparition was related to the dissolution of the last oxide layer. These sharp dips allowed to know exactly when the Si was free of oxide and their recurrence after recording a CV confirmed that this measurement regenerated a SiO_x layer (inset of Figure 7a). It makes sense as the potential applied during the CV (up to +2.9 V) largely exceeded the PP (black CVs of Figure 6). The fact that the SiO_x film etched faster after a CV than after the activation suggests that the oxide layers generated by the latter process were thicker and/or denser.

The first experiment, shown by the red curve of Figure 7a, was performed under constant illumination. Apart from the variations induced by SiO_x dissolution (*vide supra*) the OCP was relatively stable with a value comprised between +0.2 and +0.1 V. These values match very well with the value of +0.17 V determined in the red CV of Figure 6, which presents the electrochemical behavior of a photoanode after dissolution of the SiO_x layer (recorded just after the apparition of a dip). The LSVs (Figures 7c and S18) indicate that the photoanode was stable during the first 23 h, started showing signs of degradation at 25 h and was totally damaged after 27 h. This behavior is striking since, in this case, the photoanode was not anodically protected and no SiO_x preserved Si from chemical etching during more than 20 h. In order to further investigate this protective effect, activated photoanodes exposed for 30 h to the electrolyte under illumination were observed by SEM. It is remarkable to note on Figures 8c and S19 that Si did not undergo etching, as no pits were observed (the differences in NPs density and morphology will be discussed in the last part).

In order to investigate how oxidation can affect the stability, another set of experiments was carried out, in the same way as previously, except that the surfaces were polarized at +2.9 V for 1 min after each CV (Figure 7a, blue curve, CVs were recorded at the times indicated by dotted lines). Here, the OCP followed the same trend as previously, settled at +0.15 V after SiO_x dissolution and we detected degradation at 22.3 h (Figure S20). This experiment confirms that the stability at OCP is not improved by additional electrochemical oxidation, on the contrary, applying such a positive potential was found to deteriorate the stability time.

We now investigate the effect of illumination. In the last set of experiments (black curve of Figure 7a), we performed the same experiment as that shown by the red curve except that it was carried out in the dark. In this case, the first dip appeared at the same time as for the previous experiments, indicating that illumination did not affect the SiO_x etching kinetics. However, after the first CV, the OCP dropped down and stabilized at -0.15 V, very close to the value for etching Si, as shown in Figure 7b. This surface was observed at SEM (Figures 8d and S21), which clearly revealed pits on the Si surface as well as the detachment of the NPs in many areas, confirming that the electrode underwent alkaline etching after 4 h.

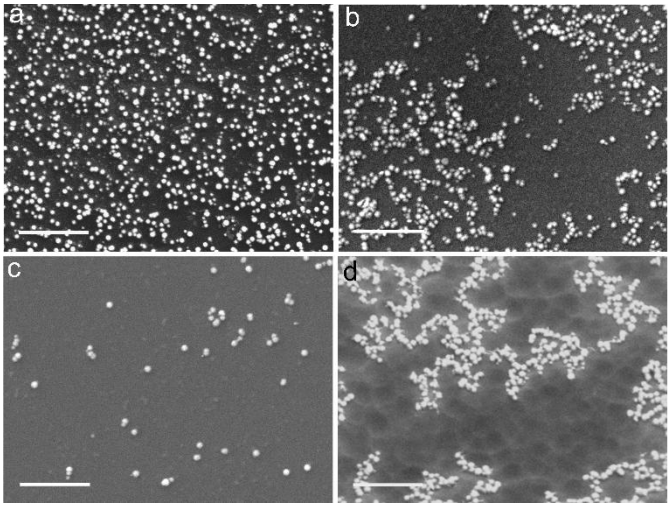

Fig. 8. SEM pictures showing top views of activated photoanodes: a) after activation, b) after 20 h of photoelectrolysis in 1 M NaOH at +1.23 V, c) after being immersed in 1 M NaOH for 30 h under illumination and d) after the OCP measurements shown in the black curve of Figure 7a. The scale bars equal 1 µm.

To sum up, this set of OCP experiments demonstrates that: *i*) illuminated photoanodes do not degrade for more than 20 h, even when oxide-free Si is in contact with the alkaline solution, *ii*) additional electrochemical oxidation of Si does not improve the stability and *iii*) the surfaces are more prone to alkaline etching in the dark. The first two points clearly reveal that the protection mechanism taking place at OCP is not related to the anodic protection occurring on operating photoanodes (*vide supra*) and the third point highlights the importance of illumination for surface stability.

Proposed mechanism for unbiased photoanodes

These results were unexpected and show that the behavior of our photoanodes is totally different from the one of Si in NaOH solutions, even though only 18 % of the surface was initially covered by the Ni NPs. We attribute the resistance towards etching to a modification of the solution-exposed Si surface. It makes sense because it is well known that small modifications in Si characteristics (*e.g.* induced by the type of dopant or its density) can have a dramatic effect on the rate of alkaline etching.[15] In our case, the electroless deposition of Ni is thermodynamically possible as the standard potential of the Ni^{2+}/Ni^0 couple (-0.26 vs NHE)[62] is more positive than the self-oxidation potential of Si (-0.99 vs NHE), therefore allowing the following overall reaction:

$$2\ Ni^{2+}\ (l) + Si\ (s) + O_2\ (g) \rightarrow 2\ Ni^0\ (s) + SiO_2\ (s) \qquad (4)$$

This is comforted by several reports by Osaka *et al.* that have demonstrated the feasibility of electroless plating of Ni on Si in alkaline media.[61,63] On the other hand, the OCP of Figure 7a was always more positive than the E_{fb} (Figure 2a and 6), which means that the electrodes at OCP during SiO_x etching were in depletion regime. This indicates that, in these conditions and under illumination, the photogenerated holes are directed to the solid-electrolyte interface where they can participate in oxidation reactions. Since the oxidation potential of $Ni(OH)_2$ is very high (> 0.8 V, as shown in Figure 6), these holes should oxidize Ni^0 rather than $Ni(OH)_2$, thus, the two following reactions may occur:

$$Ni^0\ (s) + 2\ OH^-\ (l) + 2\ h^+ \rightarrow Ni^{II}(OH)_2\ (s) \qquad (5)$$

$$Ni^0\ (s) + 2\ h^+ \rightarrow Ni^{2+}\ (l) \qquad (6)$$

Given the high pH in solution and the low solubility product constant of $Ni(OH)_2$ ($K_s \sim 10^{-16}$), the concentration of Ni^{2+} ions in solution must be very low.[64] However, this is probably different at the photoelectrode interface. In particular, we believe that the rate of reaction (6) can be considerably increased by a complexation of the Ni^{2+} ions by negatively charged species such as silicates. It is known that soluble silicates and their polymers are released during the etching of SiO_x[15] and Si[16] and they should accumulate in the Helmholtz layer for compensating the positive charge of the depleted Si, as shown in Figure 9a. Note that several examples of metal cations-silicate complexes, soluble in alkaline solution, have been reported in the literature.[65,66] Such a favorable local environment should enhance the rate of reaction (6), leading to a local enrichment of Ni^{2+} ions over the uncovered surface. As soon as Si is free of oxide (at the dips in Figure 7a), these Ni^{2+} ions can deposit on Si following the electroless reaction (4). Obviously, the so-generated Si oxide is instantaneously etched and the deposited Ni^0 is oxidized. This mechanism explains the illumination dependence of alkaline etching because no hole is generated in the dark, thus, reaction (6) cannot occur, inhibiting the Ni electroless deposition.

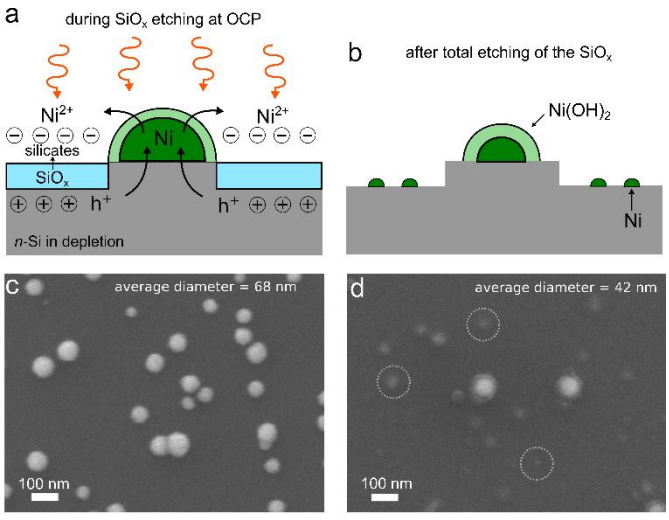

Fig. 9. a,b) Schemes depicting the electroless deposition mechanism explaining the enhanced stability of the photoanodes at OCP under illumination. c) High magnification SEM picture showing the surface of a photoanode after activation. d) High magnification SEM picture of the same photoanode after being exposed to 1 M NaOH under illumination for 15 h, for clarity 3 NPs are indicated by dashed circles.

We expect this mechanism to generate a Ni submonolayer on the Si surface (Figure 9b), that could considerably decrease the Si etching kinetics, explaining the enhanced stability at OCP under illumination. This mechanism is well corroborated by SEM observations at high magnification (Figure 9c,d) that revealed the difference in the morphology of the NPs present on an activated photoanode before and after immersion in the electrolyte at the OCP for 15 h under illumination. These images show clearly that the majority of the NPs shrunk by more than 75% of their initial volume, demonstrating their dissolution under illumination (additional SEM pictures are provided in Figures S22 and S23). In contrast, no clear change of the NPs size could be observed for electrodes that underwent alkaline etching in the dark (Figures 8d and S21). These results confirm the dissolution of the Ni NPs under illumination (reaction (6)) and support the electroless deposition-based mechanism (overall equation (4)).

Conclusions

We have reported on high-performance Si-based photoanodes, fabricated by a simple low-cost process only involving the aqueous electrodeposition of Ni NPs on *n*-Si. In spite of the notorious instability of Si in aqueous solutions and the fact that the Ni covers a very small part of the Si surface, these electrodes show striking performance for OER in alkaline electrolytes. We have presented a deep investigation of the photoelectrochemical activation, which, by generating a high-activity $Ni(OH)_2$-NiOOH catalytic shell around the Ni NPs, considerably improves the photoanode performance for OER in alkaline media. In addition, we have studied the stability of these surfaces in operation and unbiased. While the stability of operating photoanodes can be understood by anodic passivation, we showed that the stability at OCP is dependent on illumination. Our findings allowed to propose a mechanism, based on electroless deposition, explaining the resistance towards alkaline etching. The behavior of these photoelectrodes is highly intriguing and breaks with the common protection strategies based on conformal thin films. It thus opens up new opportunities that might lead to breakthrough advances in the field of photoelectrode protection.

Conflicts of interest

There are no conflicts to declare.

Acknowledgments

This work is partly funded by ANR (project EASi-NANO, ANR-16-CE09-0001-01) and has also been supported by Rennes Métropole (AIS 16C402). S. Fryars and S. Tsareva are acknowledged for valuable discussions. We are grateful to Pr. Kwabena D. Bediako, University of California, Berkeley, for the synthesis of the NiOOH phases used as references for XAS measurements.

Notes and references

1 N. S. Lewis and D. G. Nocera, *Proc. Natl. Acad. Sci.* , 2006, **103**, 15729–15735.
2 M. R. Shaner, H. A. Atwater, S. Lewis and E. W. Mcfarland, *Energy Environ. Sci.*, 2016, **9**, 2354–2371.
3 A. Rothschild and H. Dotan, *ACS Energy Lett.*, 2017, **2**, 45–51.
4 A. Fujishima and K. Honda, *Nature*, 1972, **238**, 37–38.
5 H. Gerischer, in *Solar Energy Conversion: Solid-State Physics Aspects*, ed. B. O. Seraphin, Springer, Berlin, Heidelberg, 1979, pp. 115–172.
6 M. G. Walter, E. L. Warren, J. R. McKone, S. W. Boettcher, Q. Mi, E. A. Santori and N. S. Lewis, *Chem. Rev.*, 2010, **110**, 6446–6473.
7 C. Xiang, A. Z. Weber, S. Ardo, A. Berger, Y. Chen, R. Coridan, K. T. Fountaine, S. Haussener, S. Hu, R. Liu, N. S. Lewis, M. A. Modestino, M. M. Shaner, M. R. Singh, J. C. Stevens, K. Sun and K. Walczak, *Angew. Chem. Int. Ed.*, 2016, **55**, 12974–12988.
8 K. Sivula and R. van de Krol, *Nat. Rev. Mater.*, 2016, **1**, 15010.
9 J. W. Ager, M. R. Shaner, K. A. Walczak, I. D. Sharp and S. Ardo, *Energy Environ. Sci.*, 2015, **8**, 2811–2824.
10 K. Sun, S. Shen, Y. Liang, P. E. Burrows, S. S. Mao and D. Wang, *Chem. Rev.*, 2014, **114**, 8662–8719.
11 A. J. Bard and M. S. Wrighton, *J. Electrochem. Soc.* , 1977, **124**, 1706–1710.
12 H. Gerischer, *J. Electroanal. Chem. Interfacial Electrochem.*, 1977, **82**, 133–143.
13 S. Hu, N. S. Lewis, J. W. Ager, J. Yang, J. R. McKone and N. C. Strandwitz, *J. Phys. Chem. C*, 2015, **119**, 24201–24228.
14 D. Bae, B. Seger, P. C. K. Vesborg, O. Hansen and I. Chorkendorff, *Chem. Soc. Rev.*, 2017, **46**, 1933–1954.
15 X. G. Zhang, *Electrochemistry of Silicon and Its Oxide*, Kluwer Academic, 2001.
16 E. D. Palik, H. F. Gray and P. B. Klein, *J. Electrochem. Soc.* , 1983, **130**, 956–959.
17 P. Allongue, V. Costa-Kieling and H. Gerischer, *J. Electrochem. Soc.* , 1993, **140**, 1018–1026.
18 K. Jun, Y. S. Lee, T. Buonassisi and J. M. Jacobson, *Angew. Chem. Int. Ed.*, 2012, **51**, 423–427.
19 C. R. Cox, M. T. Winkler, J. J. H. Pijpers, T. Buonassisi and D. G. Nocera, *Energy Environ. Sci.*, 2013, **6**, 532–538.
20 B. Mei, A. A. Permyakova, R. Frydendal, D. Bae, T. Pedersen, P. Malacrida, O. Hansen, I. E. L. Stephens, P. C. K. Vesborg, B. Seger and I. Chorkendorff, *J. Phys. Chem. Lett.*, 2014, **5**, 3456–3461.
21 M. J. Kenney, M. Gong, Y. Li, J. Z. Wu, J. Feng, M. Lanza and H. Dai, *Science*, 2013, **342**, 836–840.

22 K. Sun, F. H. Saadi, M. F. Lichterman, W. G. Hale, H.-P. Wang, X. Zhou, N. T. Plymale, S. T. Omelchenko, J.-H. He, K. M. Papadantonakis, B. S. Brunschwig and N. S. Lewis, *Proc. Natl. Acad. Sci. USA*, 2015, **112**, 3612–3617.

23 B. Guo, A. Batool, G. Xie, R. Boddula, L. Tian, S. U. Jan and J. R. Gong, *Nano Lett.*, 2018, **18**, 1516–1521.

24 A. G. Scheuermann, J. P. Lawrence, K. W. Kemp, T. Ito, A. Walsh, C. E. D. Chidsey, P. K. Hurley and P. C. McIntyre, *Nat. Mater.*, 2016, **15**, 99–105.

25 S. Hu, M. R. Shaner, J. A. Beardslee, M. Lichterman, B. S. Brunschwig and N. S. Lewis, *Science*, 2014, **344**, 1005–1009.

26 L. Chen, J. Yang, S. Klaus, L. J. Lee, R. Woods-Robinson, J. Ma, Y. Lum, J. K. Cooper, F. M. Toma, L.-W. Wang, I. D. Sharp, A. T. Bell and J. W. Ager, *J. Am. Chem. Soc.*, 2015, **137**, 9595–9603.

27 T. Yao, R. Chen, J. Li, J. Han, W. Qin, H. Wang, J. Shi, F. Fan and C. Li, *J. Am. Chem. Soc.*, 2016, **138**, 13664–13672.

28 I. A. Digdaya, G. W. P. Adhyaksa, B. J. Trześniewski, E. C. Garnett and W. A. Smith, *Nat. Commun.*, 2017, **8**, 15968.

29 L. Santinacci, M. W. Diouf, M. K. S. Barr, B. Fabre, L. Joanny, F. Gouttefangeas and G. Loget, *ACS Appl. Mater. Interfaces*, 2016, **8**, 24810–24818.

30 N. S. Lewis, *Nat. Nanotechnol.*, 2016, **11**, 1010–1019.

31 G. Loget, B. Fabre, S. Fryars, C. Mériadec and S. Ababou-Girard, *ACS Energy Lett.*, 2017, **2**, 569–573.

32 J. C. Hill, A. T. Landers and J. A. Switzer, *Nat. Mater.*, 2015, **14**, 1150–1155.

33 X. Yu, P. Yang, S. Chen, M. Zhang and G. Shi, *Adv. Energy Mater.*, 2017, **7**, 1601805.

34 G. Xu, Z. Xu, Z. Shi, L. Pei, S. Yan, Z. Gu and Z. Zou, *ChemSusChem*, 2017, **10**, 2897 –2903.

35 W. J. Dong, Y. J. Song, H. Yoon, G. H. Jung, K. Kim, S. Kim and J.-L. Lee, *Adv. Energy Mater.*, 2017, **7**, 1700659.

36 K. Sun, N. L. Ritzert, J. John, H. Tan, W. Hale, J. Jiang, I. A. Moreno-Hernandez, K. M. Papadantonakis, T. P. Moffat, B. S. Brunschwig and N. Lewis, *Sustain. Energy Fuels*, 2018, DOI: 10.1039/C7SE00583K.

37 T. Han, Y. Shi, X. Song, A. Mio, L. Valenti, F. Hui, S. Privitera, S. Lombardo and M. Lanza, *J. Mater. Chem. A*, 2016, **4**, 8053–8060.

38 R. T. Tung, *Phys. Rev. B*, 1992, **45**, 13509–13523.

39 R. C. Rossi and N. S. Lewis, *J. Phys. Chem. B*, 2001, **105**, 12303–12318.

40 F. A. L. Laskowski, M. R. Nellist, R. Venkatkarthick and S. W. Boettcher, *Energy Environ. Sci.*, 2017, **10**, 570–579.

41 S. L. Medway, C. A. Lucas, A. Kowal, R. J. Nichols and D. Johnson, *J. Electroanal. Chem.*, 2006, **587**, 172–181.

42 D. S. Hall, C. Bock and B. R. MacDougall, *J. Electrochem. Soc.* , 2013, **160**, F235–F243.

43 L. Trotochaud, J. K. Ranney, K. N. Williams and S. W. Boettcher, *J. Am. Chem. Soc.*, 2012, **134**, 17253–17261.

44 D. K. Bediako, B. Lassalle-Kaiser, Y. Surendranath, J. Yano, V. K. Yachandra and D. G. Nocera, *J. Am. Chem. Soc.*, 2012, **134**, 6801–6809.

45 J. Zhao, L. Cai, H. Li, X. Shi and X. Zheng, *ACS Energy Lett.*, 2017, **2**, 1939–1946.

46 G. R. Conner, *J. Vac. Sci. Technol.*, 1978, **15**, 343–347.

47 P. J. Grunthaner, F. J. Grunthaner and J. W. Mayer, *J. Vac. Sci. Technol.*, 1980, **17**, 924–929.

48 K. S. Kim and N. Winograd, *Surf. Sci.*, 1974, **43**, 625–643.

49 M. C. Biesinger, L. W. M. Lau, A. R. Gerson and R. S. C. Smart, *Phys. Chem. Chem. Phys.*, 2012, **14**, 2434–2442.

50 X.-R. Yu and H. Hantsche, *Surf. Interface Anal.*, 1993, **20**, 555–558.

51 L. Trotochaud, S. L. Young, J. K. Ranney and S. W. Boettcher, *J. Am. Chem. Soc.*, 2014, **136**, 6744–6753.

52 H. S. Ahn and A. J. Bard, *J. Am. Chem. Soc.*, 2016, **138**, 313–318.

53 N. Li, D. K. Bediako, R. G. Hadt, D. Hayes, T. J. Kempa, F. von Cube, D. C. Bell, L. X. Chen and D. G. Nocera, *Proc. Natl. Acad. Sci.* , 2017, **114**, 1486–1491.

54 M. B. Stevens, C. D. M. Trang, L. J. Enman, J. Deng and S. W. Boettcher, *J. Am. Chem. Soc.*, 2017, **139**, 11361–11364.

55 D. A. Corrigan, *J. Electrochem. Soc.* , 1987, **134**, 377–384.

56 M. B. Stevens, L. J. Enman, A. S. Batchellor, M. R. Cosby, A. E. Vise, C. D. M. Trang and S. W. Boettcher, *Chem. Mater.*, 2017, **29**, 120–140.

57 E. D. Palik, O. J. Glembocki, I. J. Heard, P. S. Burno and L. Tenerz, *J. Appl. Phys.*, 1991, **70**, 3291–3300.

58 J. W. Faust and E. D. Palik, *J. Electrochem. Soc.* , 1983, **130**, 1413–1420.

59 E. D. Palik, J. W. Faust, H. F. Gray and R. F. Greene, *J. Electrochem. Soc.* , 1982, **129**, 2051–2059.

60 H. F. Okorn-Schmidt, *IBM J. Res. Dev.*, 1999, **43**, 326–351.

61 D. Niwa, N. Takano, T. Yamada and T. Osaka, *Electrochim. Acta*, 2003, **48**, 1295–1300.

62 A. J. Bard and L. R. Faulkner, *Electrochemical Methods Fundamentals and Applications, second edition*, John Wiley & Sons, Inc., 2001.

63 D. Niwa, T. Homma and T. Osaka, *J. Phys. Chem. B*, 2004, **108**, 9900–9904.

64 D. C. Silverman, *Corrosion*, 1981, **37**, 546–548.

65 M. R. Anseau, J. P. Leung, N. Sahai and T. W. Swaddle, *Inorg. Chem.*, 2005, **44**, 8023–8032.

66 G. S. Pokrovski, J. Schott, F. Farges and J.-L. Hazemann, *Geochim. Cosmochim. Acta*, 2003, **67**, 3559–3573.

Table of Content Graphic